



Dense Molecular Clouds in the Crab Supernova Remnant

Alwyn Wootten¹ , Rory O. Bentley², J. Baldwin³, F. Combes⁴, A. C. Fabian⁵ , G. J. Ferland⁶ , E. Loh³, P. Salome⁷,
C. N. Shingledecker^{8,9,10} , and A. Castro-Carrizo¹¹

¹National Radio Astronomy Observatory, Charlottesville, VA, USA; awootten@nrao.edu¹²

²UCLA Department of Physics and Astronomy, Los Angeles, CA 90095-1547, USA

³Physics and Astronomy Department, Michigan State University, East Lansing, MI 48864-1116, USA

⁴Observatoire de Paris, LERMA, Collège de France, PSL Univ., CNRS, Sorbonne Univ., Paris, France

⁵Institute of Astronomy, University of Cambridge, Madingley Road, Cambridge CB3 0HA, UK

⁶Department of Physics and Astronomy, University of Kentucky, Lexington, KY 40506, USA

⁷Observatoire de Paris, LERMA, PSL Univ., CNRS, Sorbonne Univ., Paris, France

⁸Center for Astrochemical Studies, Max Planck Institute for Extraterrestrial Physics, Garching, Germany

⁹Institute for Theoretical Chemistry, University of Stuttgart, Stuttgart, Germany

¹⁰Department of Physics & Astronomy, Benedictine College, Atchison, KS 66002, USA

¹¹Institut de Radioastronomie Millimétrique, 300 rue de la Piscine, F-38406 Saint-Martin-d'Hères France

Received 2021 May 28; revised 2021 November 10; accepted 2021 November 10; published 2022 January 25

Abstract

Molecular emission was imaged with ALMA from numerous components near and within bright H₂-emitting knots and absorbing dust globules in the Crab Nebula. These observations provide a critical test of how energetic photons and particles produced in a young supernova remnant interact with gas, cleanly differentiating between competing models. The four fields targeted show contrasting properties but within them, seventeen distinct molecular clouds are identified with CO emission; a few also show emission from HCO⁺, SiO, and/or SO. These observations are compared with Cloudy models of these knots. It has been suggested that the Crab filaments present an exotic environment in which H₂ emission comes from a mostly neutral zone probably heated by cosmic rays produced in the supernova surrounding a cool core of molecular gas. Our model is consistent with the observed CO $J = 3 - 2$ line strength. These molecular line emitting knots in the Crab Nebula present a novel phase of the ISM representative of many important astrophysical environments.

Unified Astronomy Thesaurus concepts: [Supernova remnants \(1667\)](#); [Molecular clouds \(1072\)](#)

1. Introduction

Massive stars explode via core collapse and ejection of surrounding layers. Large abundances of refractory elements in those layers may produce dust and molecules; these supernovae may be the dominant source of dust and molecules in the early universe (Sarangi et al. 2018). ALMA has identified CO, ²⁸SiO, and ²⁹SiO (Kamenetzky et al. 2013; Matsuura et al. 2017) as well as copious amounts of dust ($\sim 0.7 M_{\odot}$) in the core-collapse supernova 1987A inner ejecta; the mass of molecular material continues to increase as the remnant evolves. Dust ($0.1\text{--}0.6 M_{\odot}$; Barlow et al. 2010; De Looze et al. 2017) and molecules (Wallström et al. 2013) have also been observed in the more evolved (330 yr old) remnant Cas A, the remnant of a Type IIb supernova of a massive supergiant. Dust has also been measured in G54.1+0.3, which appears to have at least $\sim 0.3 M_{\odot}$ in the more evolved (1500–3000 yr old) remnant of its 16–27 M_{\odot} progenitor (Rho et al. 2018; Temim et al. 2017). Here we investigate the chemistry of a remnant of intermediate age, the Tau A remnant, the Crab, which appeared in the year 1054.

The Crab Nebula is a prime example of a nearby and easily observable though more evolved young remnant of the

common Type IIP core-collapse supernova. These SNe ejecta are efficient and productive dust sources among supernovae (Sarangi et al. 2018). The Crab is a pulsar wind nebula well known for its expanding bubble of relativistic plasma that produces strong synchrotron radiation and cosmic rays. These in turn impinge on and excite a filamentary system of condensations that have formed around the exterior of the bubble. The ionized gas in these condensations has been heavily studied with a special interest in the unusual chemical abundances produced in the SN. The molecular content of the filaments has been little explored since the discovery of relatively bright infrared lines of H₂ (Graham et al. 1990). Measurement of the molecular content can reveal gas isotopic composition, as well as details of the chemical evolution of the gas in the thousand years since the supernova. The gas chemistry traces the interaction of high-energy particles and photons with the molecular gas and may inform us how gas behaves in similar environments found in distant cool-core galaxy clusters, AGN, and in SNe found early in the history of galaxies.

Data have been obtained from a detailed, panchromatic examination of the Crab's molecular component. We used our guaranteed time on the 4 m SOAR Telescope to discover 55 individual knots that are strong sources of H₂ 2.12 μm emission (Loh et al. 2010, 2011). Our follow-up near-IR spectroscopy (Loh et al. 2012) showed that the H₂ excitation temperature is ≈ 3000 K. We assembled all pertinent HST narrow-band emission-line images as well as Spitzer and Herschel data (see examples in Figure 1). These show that the H₂ knots generally follow the optical filament system, but are associated

¹² The National Radio Astronomy Observatory is operated by Associated Universities, Inc., under a cooperative agreement with the National Science Foundation.



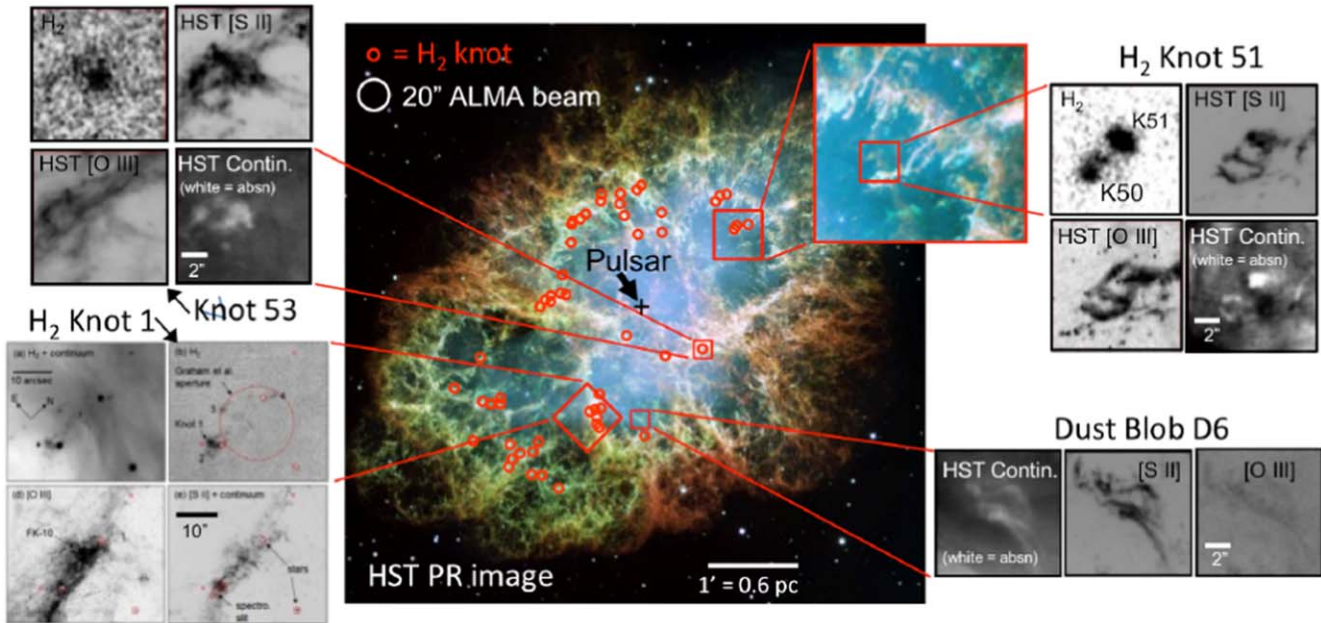


Figure 1. An image of the Crab Nebula showing 55 H₂-emitting knots measured by Loh et al. (2011) marked by red circles on the standard HST publicity image of the Crab. Insets show enlargements of our four target positions in various ground- and space-based images.

with strong low-ionization optical emission lines from which we have measured the knots' velocities.

These data constrain detailed Cloudy models (Richardson et al. 2013). The knots may be excited by synchrotron radiation, which is well constrained, or some other source of heating. The other sources of heating may be shocks or electrons and positrons from the pulsar. Priestley et al. (2017) find that a greatly enhanced cosmic-ray ionization rate, by 7 orders of magnitude, over the standard interstellar value is required to account for the OH⁺ and ArH⁺ detected lines, and lack of [C I] emission in the Herschel SPIRE FTS spectrum of the Crab (Barlow et al. 2013). The models that fit the K-band H₂ emission and optical lines show that the H₂ emission must come from what is really an extended HI zone in which a very high electron density leads to the formation of H₂ through the H⁻ route rather than in the usual way on dust. This zone is then heated, probably by cosmic rays produced in the Crab, to excite the trace amount of H₂. This is an exotic and almost completely unexplored environment for producing molecular emissions, one that we seek to characterize with ALMA observations in this paper.

To that end, we have also cataloged 280 small (arcsecond scale) absorption blobs caused by dust silhouetted against the Crab's synchrotron continuum and compared their positions to the H₂-emitting knots. Many of these were recently discussed by Grenman et al. (2017). A few H₂ knots are clearly associated with dust features, but most are not. However, the dust blobs often are associated with small knots of low-ionization gas for which we can measure velocities using our grid of optical spectra. The radial velocities show that most dust blobs are on the near side of the Crab's expanding shell, while most of the H₂ knots are on the far side. Typical extinction through the dust blobs is $A_V \sim 0.5$ mag, corresponding to $N(\text{HI}) \sim 10^{21} \text{ cm}^{-2}$ up to a few times higher. This gas has so far not been seen in either 21 cm HI emission or absorption. It would be confused with ISM emission in the LAB survey, and the published absorption maps do not cover a sufficient velocity range. Key questions include: What are the

Table 1
Project: 2015.1.00188.S Data Sets Observational Summary

Date	N_{ant}	Baselines m	PWV mm	Flux Calibrator	Flux Jy
12-Dec-15	31	15.2–7700	0.7	J0237+2848	1.48
12-Dec-15	31	15.2–7700	0.65	J0510+1800	2.6
15-Dec-15	43	15.1–6300	0.94	J0423-0120	0.62
15-Dec-15	42	15.1–6300	0.94	J0510+1800	2.6
16-Jun-16	40	16.7–783.5	0.81	J0510+1800	1.08

Note. All integration periods were 2922 ± 4 s.

physical properties of the H₂-emitting knots, including the density, temperature, and mass? What is the physics that governs molecular emission? What excites the molecular emission and what is its chemistry? What are the dust properties in this very young SN remnant? Is there also a component of cooler molecular gas? What is the connection between the dust blobs, the H₂ knots, and other molecular species such as CO? We address these issues with new data obtained with ALMA reported here.

We used ALMA to measure molecular emission from CO $J=3-2$, and from HCO⁺, SiO, and SO from four ALMA fields in the Crab Nebula (Figure 1): (1) Knot 51, a bright H₂ knot that also has dust absorption; (2) Knot 1, a bright H₂ emitting knot that does not show dust absorption; (3) Knot 53, an H₂ knot for which we have observations seeking CO $J=2-31$ using the 30 m IRAM telescope and the Plateau de Bure interferometer; and (4) as a control sample, a dust blob D6 that is not a strong H₂ emitter.

2. Observations

Observations (Table 1) were made with ALMA in the 850 μm window (Band 7) in 2015 December on four occasions using a hybrid array during a transition from an extended configuration to a compact one. These data did not meet the

Table 2
Spectroscopic Line Parameters of In-Band Emission Lines of Interest^a.

Species	Frequency (GHz)	Transition	E_u (K)	δv km s ⁻¹
CO	345.79599	3-2	33.2	0.979
SO	346.528481	8(9) - 7(8)	78.8	0.979
HCO ⁺ b	356.73422	4-3	42.8	0.979
SiO	347.33058	8-7	75	0.979

Note.

^b HCO⁺ $J = 4 - 3$ at $V_{\text{LSRK}} > 400$ km s⁻¹ fell outside the tuning band.

brightness sensitivity proposed for the observations, therefore a second set of observations was obtained 2016 June 16 in a more compact configuration (C40-4) using 40 12 m antennas deployed on baselines from 17 to 784 m. The largest scales to which the observations are sensitive are $\sim 11''$. The flux scale was set via observations of J0510+1800 ($S_{345.6\text{GHz}} = 1.08$ Jy).

Four pointings toward particular dust and/or H₂-emitting globules were made within a single session on June 16. In each pointing, four spectral windows 1.875 GHz wide were observed centered near 345 GHz to cover the four spectral lines listed in Table 2 to provide maximal continuum sensitivity and spectral grasp. The raw data were processed by the ALMA/NA Regional Center using the CASA package 4.5.3; nearby quasars were used for flux and bandpass calibration as listed in Table 1. The phase calibrator used was J0521+2112 ($S_{345.6\text{GHz}} = 200 \pm 2.4$ mJy).

CASA clean was used in the delivered data with standard robust = 0.5 weighting, tapered to $0''.45$ beam to produce data cubes matching the proposal request for locating emission lines within the $17''$ FWHP primary beam. All 1906 channels were imaged for each spectral window. The beam size of the delivered data was $0''.49$ by $0''.43$ at position angle -37° , with velocity resolutions listed in Table 2. In the delivered June 16 data, the sensitivity was 3.7 mJy in those bandwidths. Continuum sensitivity was about $75 \mu\text{Jy}$. The data was reimaged to take advantage of the higher resolution which could be realized from all the data delivered (including 2015 December data) using natural weighting, which produced a $0''.33 \times 0''.25$ beam at PA -36° at a sensitivity of 2.8 mJy beam⁻¹ or about 400 mK. It is on these images which we report.

3. Results

Molecular knots in the Crab may be identified using different tracers. The most complete description of the character of a knot includes aspects derived from all tracers. For each knot, we discuss the relationship between the various tracer components—warm H₂, dust, and target molecules—to develop a more comprehensive view of the character of the cool molecular emitting component.

3.1. Knot 51

Spatially distinct and isolated, near the tip of an inwardly reaching finger of a gas filament to the northwest of the pulsar wind nebula, this $\sim 1''$ diameter dust globule (CrN12 in Grenman et al. 2017) was modeled by Richardson et al. (2013). In this globule different tracers reveal different aspects of related spatial structures at different wavelengths. H₂ traces higher excitation neutral gas. A small H₂ radial velocity

($V_{\text{LSRK}} = 103.4 \pm 100$ km s⁻¹; Loh et al. 2012) coupled with the large transverse velocity (1340 km s⁻¹) measured for the dust knot CrN12 suggests that the knot lies near the nebular midplane, following its expansion westward in the plane of the sky, on the outskirts of the remnant (Grenman et al. 2017). Grenman et al. (2017) measured CrN12 to subtend $1''.2$ (2400 au) diameter and estimated a dust mass for it of $1.6 \times 10^{-5} M_\odot$. We clearly detect a distinct and cospatial CO emission feature from Knot 51, at $V_{\text{LSRK}} = 89$ km s⁻¹ illustrated in Figure 2, suggesting the association of CO gas with both the dust and the warmer H₂ gas. Allowing for nebular expansion of $0''.01/\text{yr}$ in the two years between the HST images of the dust knot and the ALMA observation, the integrated CO image closely follows the contours of the dust knot as seen in Figure 1, as does H₂. This, along with the kinematic evidence, suggests a close association between dust, H₂, and CO. The full velocity width to half maximum intensity of the CO feature is 5 km s⁻¹; the deconvolved size of the CO emission is $0''.46 \times 0''.41$ in a $0''.33 \times 0''.26$ beam. HCO⁺ emission was also seen from Knot 51 (Figure 3) though only limits were measured for SiO and SO. Knot 51 lies very close to Knot 50 and 52, both also sources of H₂ emission. Knot 52 (dust counterpart CrN8 in Grenman et al. 2017), with no CO counterpart, lies $\sim 5''$ to the west. The third H₂ knot, Knot 50, also without CO, lies $\sim 2''.5$ southeast of Knot 51 with the same radial velocity but its dust counterpart shows much less absorption ($A_v \sim 0.6\text{--}1.3$ mag) compared to more than 2.6 mag for Knot 51 (Richardson et al. 2013). No millimeter continuum emission was detected from the region, consistent with expectations given our sensitivity.

To try to understand the nature of Knot 51, Richardson et al. (2013) compared a number of different Cloudy models involving very different density structures and excitation mechanisms. In order to reproduce the observed H₂ intensity ratios, they found that in addition to the Crab’s synchrotron radiation field, extra heating by particles or some other source is required (their “temperature floor” and “ionizing particle” models). These models were arbitrarily truncated at the back edge of the neutral zone that produces the H₂ emission and therefore predicted very little CO emission.

However, as Richardson et al. (2013) pointed out in their Section 4.4, there could also be an extensive zone of cooler molecular gas which would produce strong CO and other molecular lines but no significant H₂. As an example, they showed some results from a representative “fully molecular core” model which did not include the extra heating sources needed to produce the observed H₂ spectrum, but which (crucially) extended to a depth (5×10^{17} cm) which was eight times greater than for the temperature floor and ionizing particles models. Their Figure 15 demonstrates the factor of $\sim 10^4$ times greater predicted strength of CO lines (relative to the already observed H₂ lines) from the fully molecular core model as compared to the temperature floor model.

The CO observations described here require a great deal more molecular gas than is present in the temperature floor or ionizing particle models. The observed integrated CO 3-2 flux is 11 K km s⁻¹. The temperature floor model predicts only 0.43 K km s⁻¹, which is about 25 times smaller than is observed, while the ionizing particle model predicts $\sim 10^6$ times less CO emission than is observed. This shows that a significant fully molecular core must be present. However, the observed H₂ emission cannot come only from a cold fully molecular region, because the accompanying CO 3-2 emission would then be far

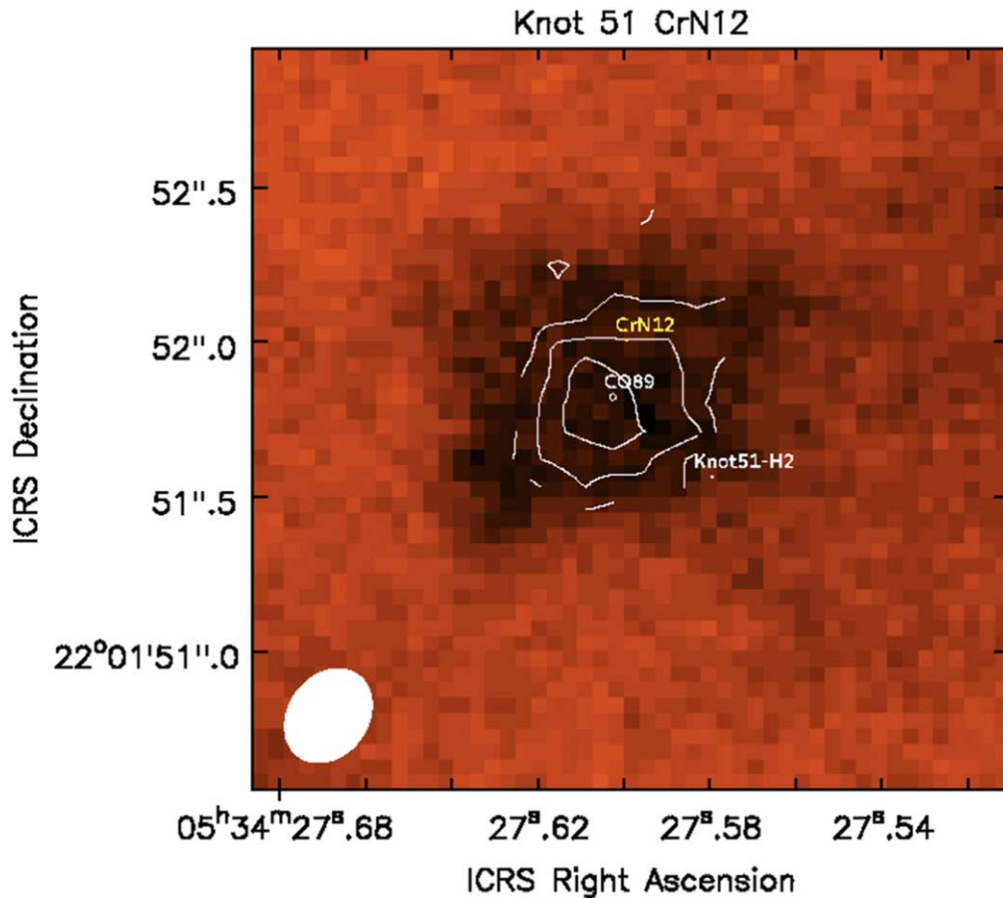


Figure 2. HST (observation GO-13510) image of the Knot 51 field with ALMA CO $J = 3 - 2$ integrated intensity image (white contours) overlaid. In the ALMA CO data, the rms is $2.8 \text{ mJy/bm km s}^{-1}$, where the beam is $0''.33 \times 0''.26$. Contours for CO emission are shown at 5σ intervals, at 5, 10, 15 σ . CrN locates dust globule position in Grenman et al. (2017); H₂ Knot 51 lies at position Knot51-H2. (Loh et al. 2011).

stronger than is observed. Therefore, the true situation must be that the observed H₂ emission comes from a thin warm layer that emits little CO, while the CO emission comes from a moderately deep molecular core behind it.

Our single observed transition of the rotational ladder does not provide strong constraints on the molecular excitation; however, the upper levels of the transitions detected in some knots (Table 1) lie between 33 and 79 K, suggesting a high excitation due to high volume density, as in the fully molecular core model. Then the CO excitation temperature should be equal to the dust temperature. The Richardson et al. (2013) model predicted grain temperatures between 38 and 54 K, which they note is in agreement with Gomez et al. (2012) who fit unresolved Herschel submillimeter emission with cold and hot dust components at 28 and 63 K, respectively, depending upon grain composition. We assume $T_{\text{ex}} = 40 \text{ K}$ in what follows, similar to the average dust temperature for the nebula of $T_{\text{dust}} = 41^{+3}_2 \text{ K}$ determined by De Looze et al. (2019). In the Richardson et al. (2013) “dense core” model, the density reaches $n(\text{H}_2) = 10^6 \text{ cm}^{-3}$, sufficient to couple gas and dust temperatures, particularly in an environment where excitation may involve electron as well as neutral particle collisions. A neutral gas temperature of $\sim 40 \text{ K}$ and density of $n \sim 10^6 \text{ cm}^{-3}$ is also consistent with excitation estimates for SN87A (Matsuura et al. 2017); the density is similar to that in the high- J CO knots in Cas A (Wallström et al. 2013). Under these conditions, the column density of CO in Knot 51 is $N(\text{CO}) = 5 \times 10^{15} \text{ cm}^{-2}$ within the measured dust core

diameter of 1200 au. Grenman et al. (2017) estimated a dust mass for CrN12 of $1.6 \times 10^{-5} M_{\odot}$. Assuming a gas to dust ratio of 100 and a mean molecular mass of 2.33, we derive a CO abundance relative to H₂ of $X(\text{CO}) = 7.6 \times 10^{-7}$, somewhat lower than commonly cited ISM values (Liszt 2007). Knot 51 also shows HCO⁺ emission; with the same excitation conditions we find an HCO⁺ column density of $N(\text{HCO}^+) = (5 \pm .4) \times 10^{12} \text{ cm}^{-2}$ and an abundance relative to H₂ of $X(\text{HCO}^+) = 7. \times 10^{-10}$, using the LTE excitation modeling program Radex (van der Tak et al. 2007). Neither SiO nor SO emissions were detected from this knot. For all molecular knots, given the excitation estimates and 3σ noise levels used here, column densities for undetected emission ($S \leq 3 \text{ mJy/beam}$) are estimated to lie below $N(\text{HCO}^+) = 5 \times 10^{11} \text{ cm}^{-2}$, $N(\text{SiO}) = 3 \times 10^{13} \text{ cm}^{-2}$, and $N(\text{SO}) = 2 \times 10^{13} \text{ cm}^{-2}$.

3.2. Knot 1

Located directly on a very bright filament on the opposite (eastern) side but not so far ($\sim 0.6 \text{ pc}$) in projection from the pulsar emission nebula as Knot 51, Knot 1 is a complex, bright H₂ emitting knot (Loh et al. 2010) that does not have clear dust absorption in the Hubble continuum images. It is the brightest H₂ knot in the Loh catalog (Loh et al. 2011) and among the largest, extending $5'' \times 2''$ approximately along an EW axis. Knot 1 covers about four times the area of Knot 51 in H₂ emission. The H₂ radial velocities (heliocentric) were measured to be $145 \pm 100 \text{ km s}^{-1}$ (Loh et al. 2012). The positive

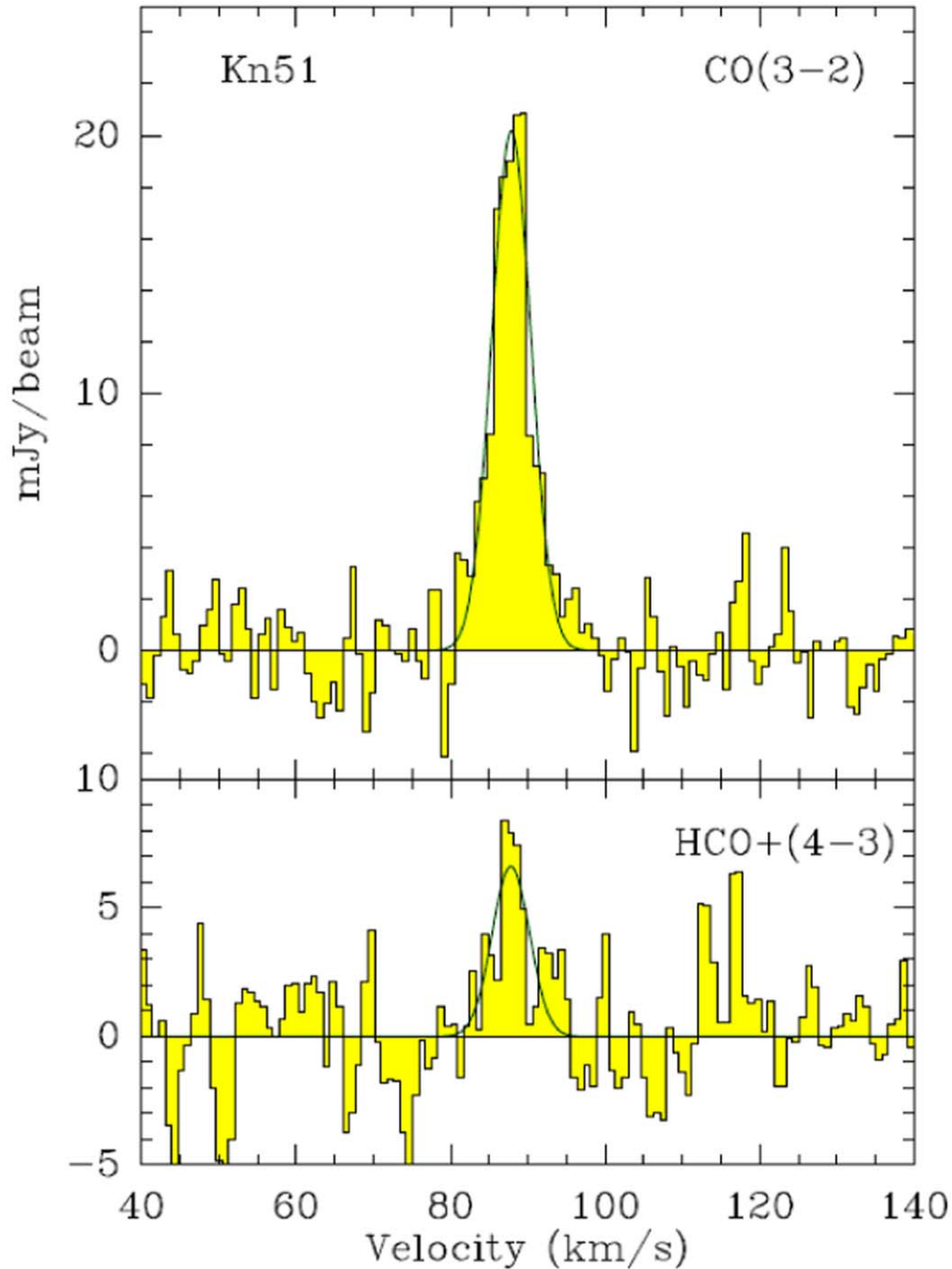


Figure 3. The spectra of CO $J = 3 - 2$ (upper) and HCO⁺ $J = 4 - 3$ (lower) are shown for the position marked CO89 in the previous figure.

recession velocities suggest that from our viewpoint the material in Knot 1 lies on the far side of the remnant, illuminated on its face by the pulsar wind nebula, consistent with the absence of clear dust absorption. Barlow et al. (2013) reported OH⁺ and ArH⁺ in this general vicinity (ArH⁺ occurred at $V_{\text{helio}} = 140 \pm 34 \text{ km s}^{-1}$, quite similar to the H₂ in the stronger Knot1NW component).

ALMA imaged three prominent distinct CO spatio-kinematic components in Knot 1 at radial velocities of $V_{\text{LSRK}} = 96 \text{ km s}^{-1}$, $V_{\text{LSRK}} = 183 \text{ km s}^{-1}$, and $V_{\text{LSRK}} = -16 \text{ km s}^{-1}$ as listed in Table 3 and illustrated in Figure 4. All components lay spatially and kinematically separated within a roughly 3'' by 3'' region in the center of the field, roughly centered on the location of Knot

1 in H₂, suggesting a physical association with that emission. Line widths (FWHM) range up to $\sim 40 \text{ km s}^{-1}$, six times those observed in Knot 51. Each component is distinct in its spatial and velocity characteristics suggesting that the three emitting regions lie separated along the line of sight within a complex structure. The northwestern component is the stronger and consists of two intermingled subcomponents oriented NE-SW with slightly more positive velocities to the SW; the variation is much less than the line width. On the basis of position, CO integrated strength, and velocity, we suggest Knot1NW-CO +96 is probably most closely associated with the H₂ cloud. Loh et al. (2012) estimated a lower limit to the H₂ molecular mass of $5 \times 10^{-5} M_{\odot}$.

Table 3
Molecular Features in the Crab SNR^{a,b}

Field	RA J(2000.0)	Decl. J(2000.0)	Velocity km s ⁻¹	Width km s ⁻¹	Int. Flux K km s ⁻¹	FWHM arcsec	N(X) cm ⁻²	M(H ₂) 10 ⁻⁴ M _⊙
Knot51/H ₂ /CrN12/89	5:34:27.603	22:01:51.81	89.	5	11	0.4	(5.5 ± 0.2) · 10 ¹⁵	1.7
Knot53/CrN17/-630	5:34:29.355	22:00:26.85	-630	30.	30	0.4	(1.5 ± .05) · 10 ¹⁶	6.7
Knot53/CrN18/-590	5:34:29.417	22:00:30.68	-590	1.6	2.4	0.5	(1.2 ± 0.5) · 10 ¹⁵	0.6
Knot53/CrN20W/-539	5:34:29.568	22:00:28.11	-539	11.7	33	0.5	(1.6 ± 0.7) · 10 ¹⁶	8.4
Knot53/CrN20E/-534	5:34:29.790	22:00:27.38	-534	14.3	54	0.6	(2.8 ± 1.3) · 10 ¹⁶	14.3
Knot53/CrN22/-496	5:34:29.633	22:00:28.75	-496	8.1	25.9	0.6	(1.3 ± 0.2) · 10 ¹⁶	6.1
Knot53/CrN16/-408	5:34:29.260	22:00:29.91	-408	8	32.	0.9	(1.7 ± 0.1) · 10 ¹⁶	88.4
Knot53/+286	5:34:28.531	22:00:34.6	286	3	18	0.5	(9.5 ± 1.0) · 10 ¹⁵	4.5
Knot53/+532	5:34:28.479	22:00:33.09	532	9	17.5	0.4	(2.9 ± 1.4) · 10 ¹⁶	3.0
Knot53/+540	5:34:28.457	22:00:32.47	540	11	70	0.4	(3.8 ± 0.3) · 10 ¹⁶	8.4
Knot53/H ₂ /+591	5:34:29.288	22:00:29.65	591	5.6	21.	0.8	(7. ± 0.5) · 10 ¹⁵	14.8
Knot1-CO-16	5:34:34.40	21:59:41.67	-16	15	20	0.5	(9.0 ± 0.3) · 10 ¹⁵	4.2
Knot1NW-CO+96	5:34:34.250	21:59:40.68	96	28	98	1.3	(5.0 ± 0.3) · 10 ¹⁶	142.
Knot1E-CO+183	5:34:34.398	21:59:40.00	183	15	45	1.8	(2.3 ± 0.1) · 10 ¹⁶	143.
D6-CO-429	5:34:32.30	21:59:37.24	-429	5	13	0.3	(6.3 ± 0.1) · 10 ¹⁵	1.1
D6-CO-521	5:34:32.231	21:59:43.22	-521	7	4.3	0.3	(2.0 ± 0.4) · 10 ¹⁵	0.37
D6/CrN45-CO-337	5:34:32.913	21:59:44.58	-337	4.5	15	1.1	(7.5 ± 0.2) · 10 ¹⁵	17.8
Knot51/CrN12/-HCO ⁺ 89	5:34:27.603	22:01:51.80	87.5	5	5.5	0.4	(5.0 ± 0.4) · 10 ¹²	
Knot53/CrN16-HCO ⁺ -408	5:34:29.25	22:00:30.1	-408	8.1	8.1	0.9	(8.0 ± 0.4) · 10 ¹²	
Knot1NW-HCO ⁺ +96	5:34:34.256ck	21:59:40.99	94.	40	50	0.8	(4.5 ± 0.1) · 10 ¹³	
Knot1E-HCO ⁺ +183	5:34:34.387ck	21:59:40.19	182	25	45	0.5	(4.4 ± 0.1) · 10 ¹³	
Knot1NW-SiO +96	5:34:34.256ck	21:59:40.99	94.	40	50	0.8	(2.0 ± 0.1) · 10 ¹⁵	
Knot1E- SiO +183	5:34:34.387ck	21:59:40.19	182	25	45	0.5	(1.8 ± 0.1) · 10 ¹⁵	
Knot1NW-SO +96 8 ₉ - 7 ₈	5:34:34.256	21:59:40.99	96.	20	13	0.8	(5.0 ± 0.5) · 10 ¹⁴	
Knot1E-SO +183 8 ₉ - 7 ₈	5:34:34.387	21:59:40.19	183	22	11	0.5	(9.0 ± 0.1) · 10 ¹²	

Notes.

^a H₂ masses have been derived, assuming CO/H₂ = 1 · 10⁻⁵, an average for the seven globules with both dust mass and CO column density measured.

^b The globule properties were derived from observations reported here, along with H₂ and optical observations. Values reported in this table are for beam averaged values at the position given. Column densities are derived using Radex, a molecular excitation fitting program, using the robust excitation (Tx=40 K, density ≈ 10⁶ cm⁻³ suggested by our detection of high-excitation transitions, and by Richardson et al. (2013).

We assume an excitation temperature for the molecules in Knot 1 as in Knot 51. We estimate CO columns for the three molecular components as listed in Table 3, from 0.8 to 4 × 10¹⁶ cm⁻²; Knot1NW-CO+96 is the most prominent of these.

Lacking dust absorption measurements, the total dust column in Knot 1 cannot be as well-characterized as it is in Knot 51. Loh et al. (2012) estimated that the total H₂ mass in Knot 1 could be 0.05 M_⊙, corresponding to a dust mass which might be detectable as thermal dust emission in our observations. In fact, our slightly tapered continuum image (0".71 × 0".64 at PA -29.50 deg) for Knot 1 clearly showed continuum emission from the location of the H₂ over a region of similar extent to that subtended by the CO emission, at least for Knot1NW and Knot1E. However, even using the more favorable gas to dust ratio of Owen & Barlow (2015) the continuum flux translates to about 4 solar masses. This is unrealistic given the mass of the progenitor star. It is likely dominated by synchrotron emission. Indeed, we detect for the two globules Knot1NW and Knot1E, over a surface of 40 beams, (or 3.6 · 10⁻⁴ pc²), a total integrated continuum emission S_{870μm} = 25 mJy ± 12 μJy. The detected continuum is probably dominated by synchrotron emission by a factor ~100, since the emission is too strong to be produced by dust. Such nonthermal emission is expected since these globules belong to a conspicuous radio/optical filament. Knot 1 appears to be the most massive observed knot, as suggested by its H₂ or CO line fluxes. It shows the brightest emission from each of the other

molecules within the band, characterized in Table 3. Why are there continuum knots? ALMA observations of the 100 GHz continuum with a lower resolution (Dubner et al. 2017) reveal multiple inhomogeneities, corresponding to plasma confined to magnetic field lines, including wisps, arches, and loops. Lacking a clear radio counterpart or optical absorption, the dust mass of Knot 1 remains uncharacterized.

The 96 km s⁻¹ (NW) and the 183 km s⁻¹ (E) components both showed emission from SiO J = 8 - 7, SO 8(9)-7(8), and HCO⁺ J = 4 - 3. In Knot1NW the SiO emission originates from the same region at the same velocity (Figure 5); however, HCO⁺ emission centers about 1000 au NNE of CO and SiO. Emission from all molecules is coincident in the E component. Assuming the same excitation for all four molecules, we obtain the molecular column densities as listed in Table 3.

3.3. Knot 53

Knot 53 is located closest in projection from the pulsar, and as might therefore be expected, lies within a region of complexity and brightness exceeded only by the region around Knot 1. Knot 53 had previously been the target of CO J = 2 - 1 observations from the IRAM 30 m telescope and the Plateau de Bure interferometer. The noise level was rms 5 mJy in 2.5 km s⁻¹ channels at 230 GHz, three times higher than the ALMA rms at 345 GHz. The nondetection is compatible with the present ALMA results since the expected CO(2-1) signal is lower by at least a factor 2 with respect to the CO(3-2) signal

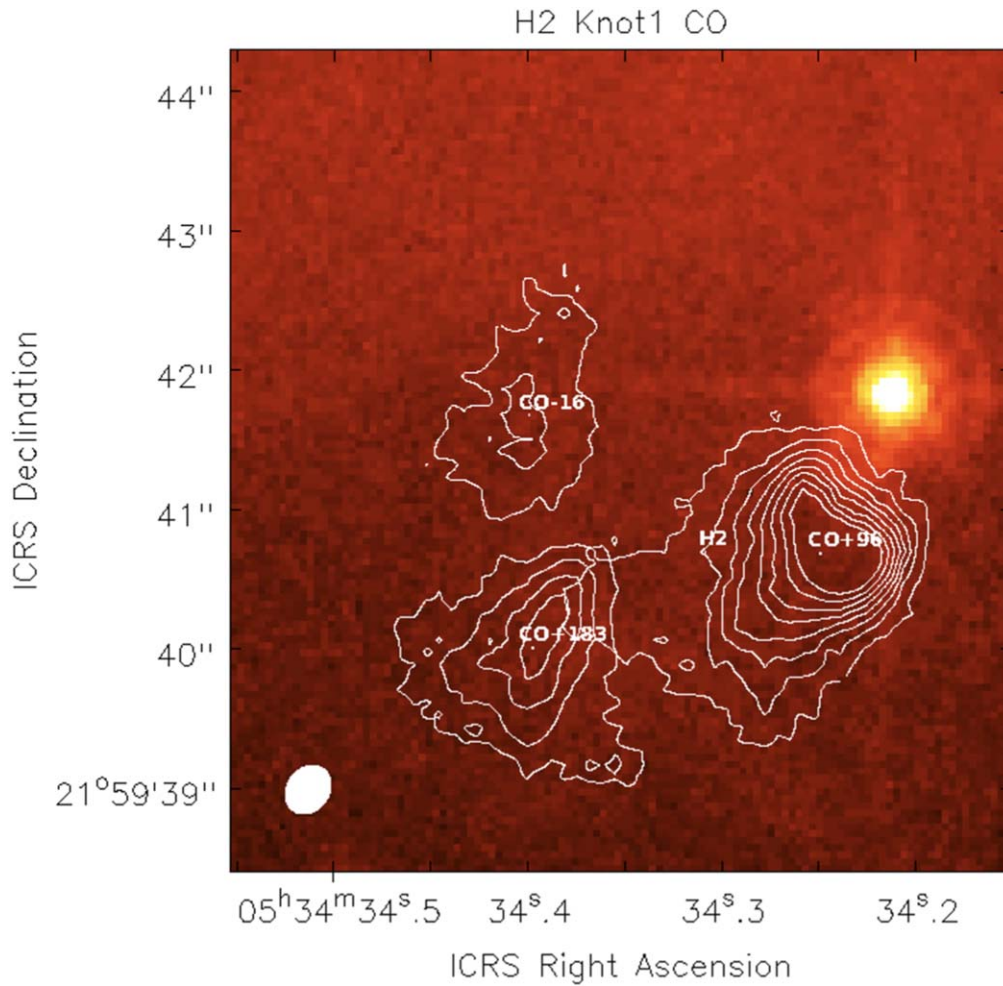


Figure 4. HST (observation GO-13510) image of the Knot 1 field with ALMA moment 0 images of CO (contours) superposed. The lowest contour is at $0.08 \text{ Jy } \text{bm}^{-1} \text{ km s}^{-1}$ and contour intervals are $0.16 \text{ Jy } \text{bm}^{-1} \text{ km s}^{-1}$. The weaker CO line at $V_{\text{LSRK}} = -16 \text{ km s}^{-1}$ has been Hanning smoothed for this image.

(Salome et al., private communication). This expected signal is assuming a dense molecular core, and a CO excitation temperature coupled to the dust temperature of 35–40 K. This is consistent with the fully molecular core model of Richardson et al. (2013). Knot 53 is situated at the western head of a trail of dust knots seen in the HST image, which mark the loci of a major filament (“E” in the Hester et al. 1990 notation) in the Crab. The unresolved filament is also seen in Herschel images (De Looze et al. 2019). There are several dense gas tracers identified within the ALMA primary beam, which targeted relatively strong molecular hydrogen emission at $V_{\text{helio}} = 696 \text{ km s}^{-1}$ ($V_{\text{LSRK}} = 668 \text{ km s}^{-1}$). Barlow et al. (2013) detected $\text{ArH}^+ J=1-0$ in detector C3 at $V_{\text{helio}} = 933 \pm 33 \text{ km s}^{-1}$ and $\text{ArH}^+ J=2-31$ in D4 at $743 \pm 26 \text{ km s}^{-1}$ in this direction. H_2 and ArH^+ are probably associated with a particular far-side CO element, Knot53/ H_2 /+591. CO emission in this region arises from two kinematic components, the molecular hydrogen emission component Knot53/ H_2 /+591 and a CO feature at $V_{\text{LSRK}} = -408 \text{ km s}^{-1}$, on opposite sides of the Crab at velocities separated 1000 km s^{-1} along one line of sight but less than half an arcsec in the projected distance apart (Figure 6). CrN16 is a prominent dust globule coincident with the CO feature, for which Grenman et al. (2017) estimated a dust mass of $5.8 \times 10^{-5} M_{\odot}$ within a radius of $2''$ (2000 au). Grenman et al. (2017) measured proper motion for the dust globules in this region; the expansion of the nebula moves them

generally southwestward with time. Between the Grenman et al. (2017) measurements in 2014 and the ALMA observations in mid-2016, all Knot 53 features are expected to have moved $0''.14$ generally along position angle 99° , consistent with the differences we observe between dust and CO gas. Positional coincidence suggests that the CO feature at -408 km s^{-1} arises within CrN16. An HCO^+ emission peak also coincides with CrN16 in position and velocity (Figure 7).

In all, ten CO features lie within the Knot 53 field, with radial velocities between $V_{\text{LSRK}} = -620.2 \text{ km s}^{-1}$ and 601.5 km s^{-1} ; seven are shown in Figure 6, spread across a portion of the ALMA field of view. Six of these show approaching velocities, centered east of Knot53- H_2 , along the trail of dust features, spanning $\sim 5''$ with velocities between -630 and -408.0 km s^{-1} . Knot53/CrN16/-408 lies at the western end of this chain.

We further identify CrN20 in Grenman’s list as the host dark cloud for the CO emission feature at $V_{\text{LSRK}} = -539 \text{ km s}^{-1}$ (W). CO within a nearby distinct cloud to the east lies at $V_{\text{LSRK}} = -534 \text{ km s}^{-1}$ associating with very weak dust absorption uncatalogued by Grenman. Dust globule CrN22 associates with CO at $V_{\text{LSRK}} = -496 \text{ km s}^{-1}$. Some prominent dark globules have no apparent CO emission—for example, CrN18 is quite prominent but the only nearby CO, that at $V_{\text{LSRK}} = -591 \text{ km s}^{-1}$, appears to be associated only with a small uncatalogued globule to its NE. Even smaller CrN17 is,

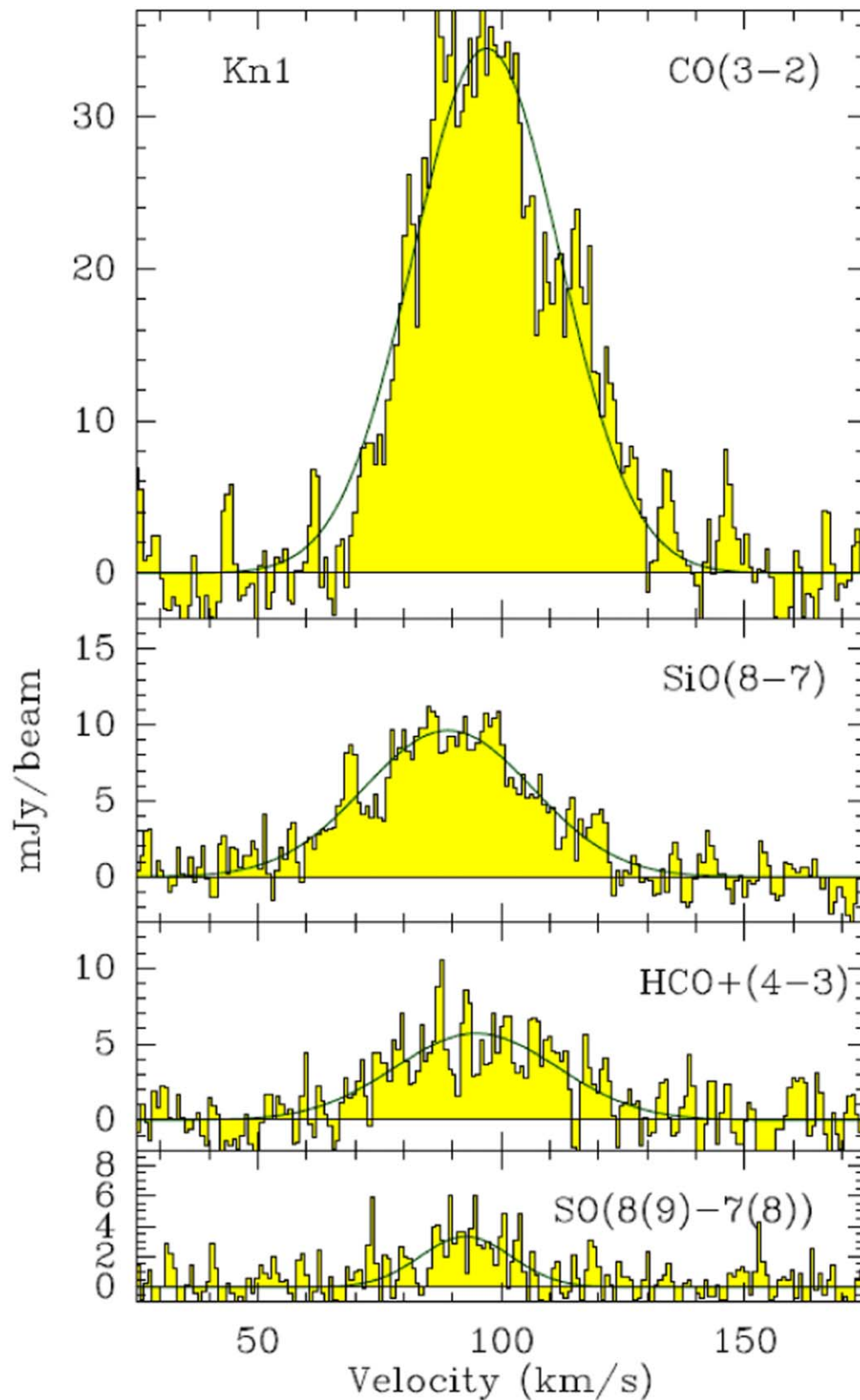


Figure 5. Profiles of the strong 96 km s^{-1} lines in Knot 1: CO (3 – 2), SiO (8-7), HCO⁺(4-3), and SO(8(9)-7(8)).

however, probably associated with weak broad CO emission near $V_{\text{LSRK}} = -630 \text{ km s}^{-1}$.

Three CO features with receding velocities lie in the far western portion of the field out of the Figure 6 field. Knot53-CO+532 and

Knot53-CO+540 lie west of Knot53-CO+286, oriented along PA 40 with V 530 in the NE increasing to 544 in the SW, broad and perhaps splitting in the SW. These are SW of the main pulsar wind nebula with no clear associated features in the HST image.

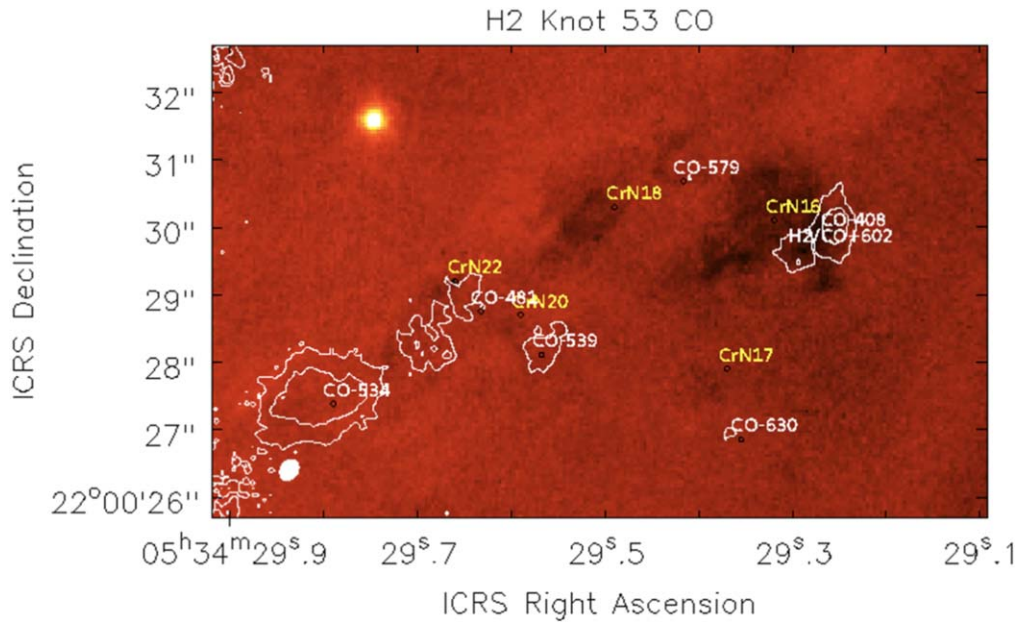


Figure 6. (L) HST (observation GO-13510) image of the Knot 53 field stretched to emphasize the globules. ALMA moment 0 images of the various CO $J = 3 - 2$ velocity components are overlaid. CO- labels indicate different velocities. White shows receding gas, in particular the 602 km s⁻¹ emission associated with the H₂ Knot 53; the nearby yellow shows the approaching gas at -408 km s⁻¹ emission associated with dust knot CrN16. In the ALMA data, the rms is 2.8 mJy bm⁻¹ km s⁻¹, where the beam is $0''.33 \times 0''.26$; for that beam, the rms is about 0.27 K in brightness temperature. Contours are shown at 45σ intervals. CrN locates absorbing dust positions in Grenman et al. (2017); H₂ Knot 53 lies at position H₂/CO+602.

In summary, of the ten CO clouds we find in the Knot 53 field, six at positive velocities can reasonably be associated with near-side dust globules cataloged in Grenman et al. (2017), one cloud probably relates to the far-side H₂ and ArH⁺ emission. Three at negative velocities seem unrelated to dust absorption in HST images or to H₂ emission.

Figure 7 shows spectra of CO and HCO⁺ toward the prominent CrN16 absorbing cloud. We assume an excitation for the molecules in each of the Knot 53 clouds as in Knot 51. As before, we use the Grenman et al. (2017) dust mass and size estimates to derive a column density for H₂ which can then be compared to the CO column to provide an estimate of the CO abundance. For instance, for CrN16, we estimate $N(\text{H}_2) = 2.7 \times 10^{22} \text{cm}^{-2}$ and thus derive a CO abundance relative to H₂ of $X(\text{CO}) = 7 \times 10^{-7}$, similar to CrN12 but lower than commonly cited values for Galactic clouds (e.g., Liszt 2007).

3.4. Knot D6

D6 lies somewhat more distant (~ 0.8 pc) in projection from the pulsar than other targeted features. H₂ was not detected toward D6 by Loh et al. (2011). Several dust features festoon the region, which includes features denoted as CrN 39, 40, 41, and 45 by Grenman et al. (2017), with transverse velocities between 200 and 500 km s⁻¹. None of the knots tabulated in that study coincide exactly with the dust feature D6 which sprawls around a small central CO feature, which has a velocity of $V_{\text{LSRK}} = -521$ km s⁻¹ on the approaching side of the nebula (Figure 8, Figure 9). Barlow et al. (2013) detected ArH⁺ $J = 2 - 1$ at $V_{\text{helio}} = 572 \pm 25$ km s⁻¹ near D6, perhaps associated with the same feature. In the eastern part of the field, the CO feature at $V_{\text{LSRK}} = -337$ km s⁻¹ lies about one synthesized beam southwest of the HST image location of dust globule CrN45 (Figure 10). Both that dust feature and the CO feature are similar in size, $\sim 0''.5$, slightly elongated in a SE–

NW direction. The offset of the centroids of the two features is consistent with the expected proper motion. We identify CrN45 with the CO cloud on this basis. A third CO feature was also detected south of the central D6 dust feature at $V_{\text{LSRK}} = -429$ km s⁻¹ but without apparent dust absorption in the HST image.

No emission was detected from HCO⁺, SiO, or SO toward any of the CO clouds in the D6 field. We assume an excitation for the CO molecules in each of the clouds as in other knots. As before, we use the Grenman et al. (2017) dust mass and size estimates to derive a column density for H₂ which can then be compared to the CO column to provide an estimate of the CO abundance for the only cloud with CO and well-characterized dust, CrN45. There we estimate $N(\text{H}_2) = 4.1 \times 10^{20} \text{cm}^{-2}$ and $N(\text{CO}) = 5.5 \times 10^{15} \text{cm}^{-2}$ thus deriving a CO abundance relative to H₂ of $X(\text{CO}) = 2 \times 10^{-5}$, somewhat higher than in the previous knots where CO abundance could be derived.

4. Discussion

Perhaps the simplest of the fields is that of the isolated Knot 51, the subject of some previous modeling by Richardson et al. (2013). The rough H₂–CO positional agreement does not suggest that the H₂ and CO emission come from a spatially identical region. The most likely geometry is one where H₂ comes from very warm gas near the surface of the globule, since temperatures approaching 3000 K are needed to excite H₂ (Ferland et al. 2008), while the CO originates in a much colder molecular core. The molecular hydrogen mass given in the last column of Table 3 is the mass of the unobserved cold H₂ that is cospatial with the CO. Their models required that the surface have an additional source of heating, which is almost certainly energetic particles (Richardson et al. 2013; Priestley et al. 2017). CO observations did not exist at that time so their comments on CO emission are parenthetical and not the result of directed modeling. Table 4 provides estimates of CO,

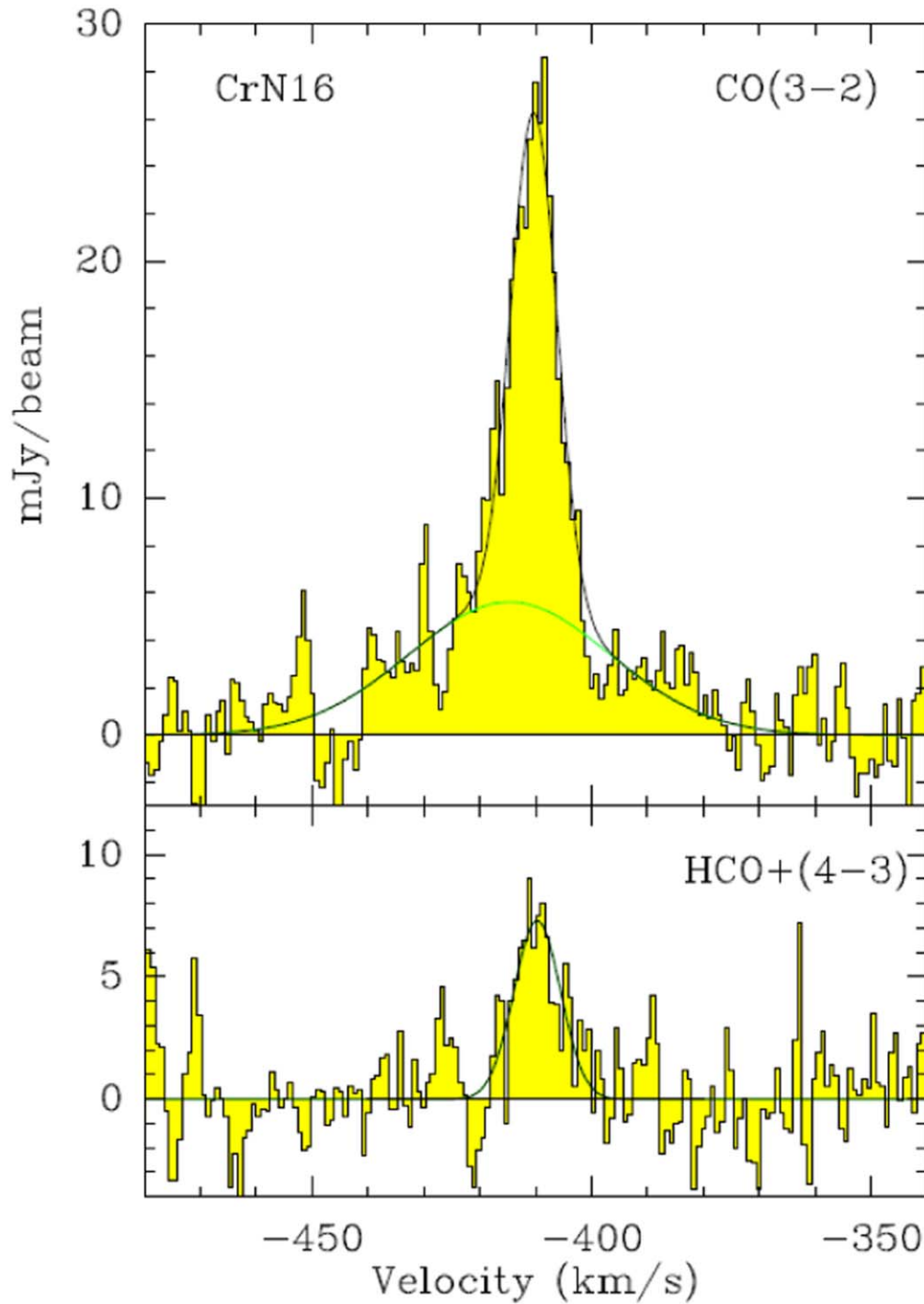


Figure 7. Profiles of CO $J = 3 - 2$ and HCO^+ $J=4-3$ emission toward the CrN16 molecular emission peak. The CO(3-2) spectrum is composed of a main component at -410 km s^{-1} (FWHM = $10. \text{ km s}^{-1}$, max = 21 mJy) which closely corresponds in extent with the dust extinction clump, and several nearby clumps without clear dust extinction counterparts, fitted by a wider Gaussian, centered at -415 km s^{-1} , and of FWHM of 42 km s^{-1} (with a maximum at 5.6 mJy).

HCO^+ , and SiO abundances for the seven globules where those molecules are observed which also have H_2 masses from Grenman’s dust measurements and where the extent of the molecular emission is the same as Grenman measured for dust.

A variety of clouds are seen. Seventeen globules have CO emission, others have CO and H_2 , and seven have CO emission with associated dust. Of the 17 CO emission regions we have described (Table 3), 10 occur in regions of dust absorption. These must occur on the near side of the nebula, both to absorb the synchrotron continuum and to account for the fact that nine

have negative CO velocities. Four CO clouds also show H_2 emission at positive velocities but lack dust absorption. Since H_2 emission also occurs at positive velocities, these clouds must lie on the far side of the expanding nebula. Four CO clouds have neither clear H_2 emission nor dust absorption.

The distribution of CO emitters is symmetric in velocity suggesting that ALMA detects most of the clouds within the Crab in its limited field of view. The H_2 clouds are mostly receding (Loh et al. 2011) suggesting that typically these have a large enough column density to extinguish the 2 micron

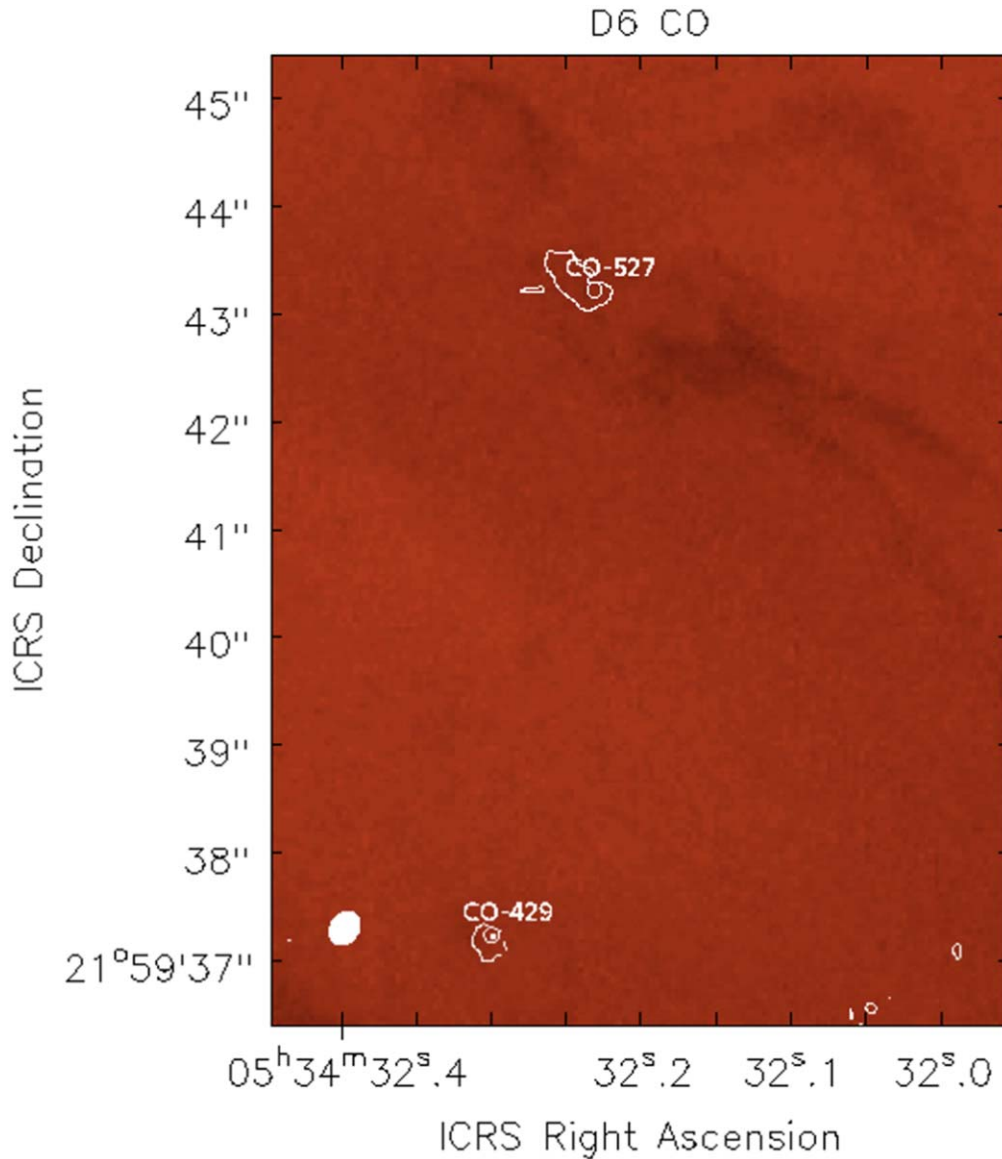


Figure 8. HST (observation GO-13510) image of the D6 field with ALMA moment 0 images of two of the CO velocity components overlaid. Contours are as in Figure 2.

emission and hide the H_2 from our vision. It follows that the extra heating needed to produce the H_2 emission must predominantly deposit energy in the side of the globule facing the pulsar wind nebula.

The dust masses and column densities listed in Tables 3 and 4 have significant, factors of ~ 2 , uncertainties. The Crab Nebula is chemically inhomogeneous with some regions having an especially high helium abundance. The grain material depends on the chemistry of the cold molecular gas in which it forms and the grain size distribution, which determines its reddening, depends on the grain formation/destruction history. Despite this, the evidence suggests that the dust in the cores is similar to ISM grains. Although there are models for each of these processes, they are not robust and depend on many parameters. Grenman et al. (2017) derived dust masses from A_V measurements. The extinction law for dust grains in these globules matches a normal interstellar extinction law. This is evidence for a globule composition similar to normal interstellar grains. We note that the ALMA

observations detect mainly the small globules and not the larger filaments which have been studied by Herschel. It would not be surprising if the dust in the globules and filaments were different and this introduces a further uncertainty in our analysis. We provide these column densities from Grenman et al. (2017) for each absorbing globule to determine a point of reference; for Knot 1, with neither dust absorption (it is on the nebular far side) nor emission, only molecular column density is measured.

The fact that the Crab Nebula is young and not interacting with the ISM eliminates one major area of uncertainty, but also important is the fact that both the fluxes and energy distribution of locally generated cosmic rays have likely not been significantly modified due to the interaction with ISM and can thus be estimated fairly well (Ivlev et al. 2018; Padovani et al. 2018). The summary of molecular column density (Table 4) suggests an elevated HCO^+ abundance in Knot 51 with respect to Knot 53, which may suggest changes in ζ , but further observations are needed to secure this hint.

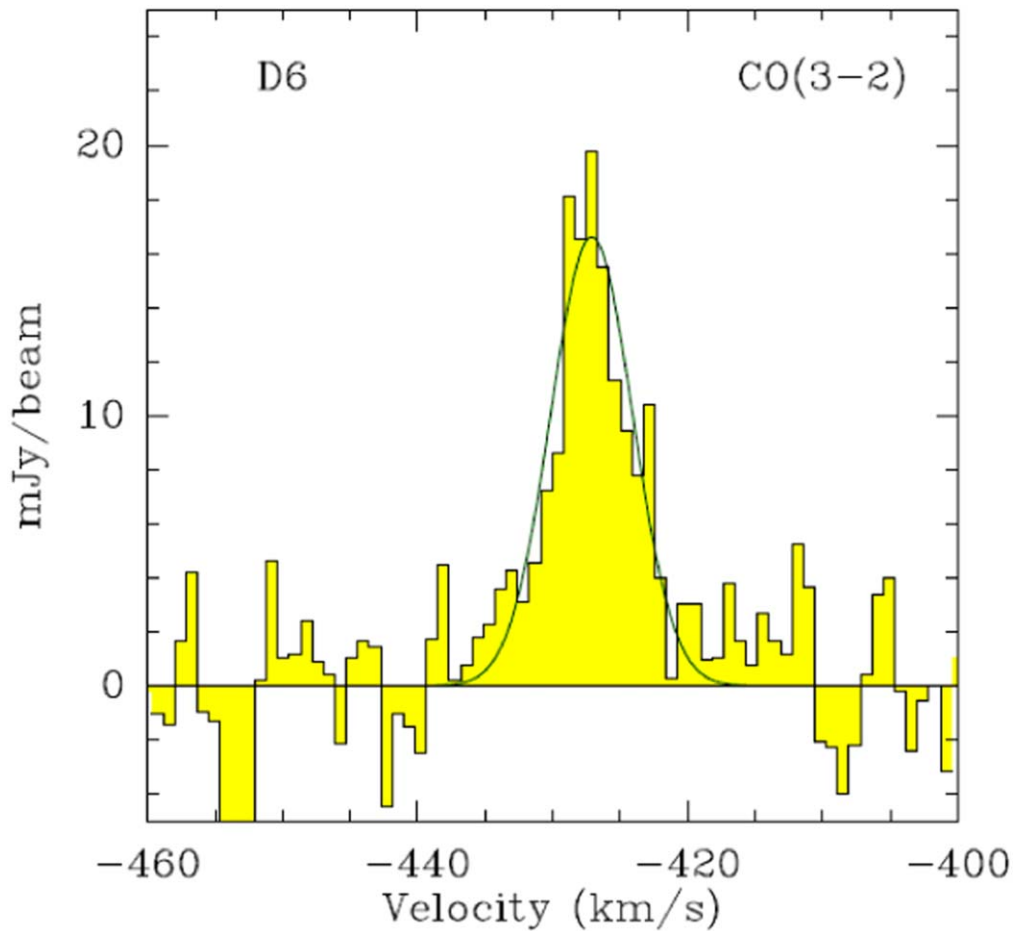


Figure 9. Profile of the $V_{\text{LSRK}} = -427$ /kms CO component toward D6.

5. Summary

Spurred by Richardson et al. (2013) who present a range of models for knots observed in the Crab, particularly the “fully molecular core” model of Knot 51, we have undertaken a small survey. We have imaged four $17''$ fields of the Crab supernova remnant selected for H_2 emission and/or apparent dust absorption with ALMA, with spectral windows covering emission from CO, HCO^+ , SiO, and SO emitting in the $850 \mu\text{m}$ window. Localized emission is found from seventeen clouds, typically under 1000 au in size, in the CO molecule. Four knots show HCO^+ emission. In H_2 Knot 1, at both of the locations and velocities of two CO clouds all four molecules—CO, HCO^+ , SiO, and SO are detected. These observations favor the “fully molecular core” model applying to a range of knot configurations. In this fully molecular core model, the emission of H_2 , CO, and other molecules does not come from the same region. CO (and HCO^+ , SiO, SO) emission occurs in the globule core, and H_2 on the surfaces. H_2 emission requires high temperatures suggesting cosmic-ray excitation. Inside dense globules, the gas is cooler, H_2 may be present, but only the CO emission will be visible.

Our ALMA observations of Knot 51 show that a significant column density of molecular gas must be present, in addition to the thin skin that produces the H_2 . Figure 15 of Richardson et al. (2013) shows that the molecular emission produced by the fully molecular core discussed in their paper is far more intense than their competing temperature floor model that was optimized to reproduce only the H_2 observations. The H_2

emission originates in a warm skin so does not require an extensive fully molecular core. Our CO observations strongly support the fully molecular core for Knot 51 since a large column density of molecular gas is needed.

A new generation of spectral models is needed to really harvest the information in the current data set or uniquely determine the energy source of the molecular regions. The Richardson et al. (2013) models focused on the remarkably strong H_2 emission. Little was known of the CO spectrum so it was a parenthetical effort in that work. As a result, these models were not optimized to determine the energy source for the molecular core using the lines ALMA has detected. There have also been significant advances in the chemistry (Shaw et al. 2020; Shaw & Ferland 2021 and in preparation), and observations of molecules such as ArH^+ are now available. A new unified modeling and observational effort may be able to discern between such competing energy sources as penetrating energetic particles or shocks.

The emitting regions encompass portions of a variety of structures observed at other wavelengths. Three (H_2 Knots 1, 51, and 53) were selected as associated with known sources of molecular hydrogen emission. CO was found to be associated with (but not cospatial with) H_2 in each of these; notably Knot 1 harbors three CO features, two of which also emit in the HCO^+ , SiO, and SO lines; all are less extensive than the warm H_2 emission. Of the latter two, Knot1NW-CO+96 is the more massive but both may contribute to the H_2 cloud. We note that a line survey of the much younger SN1987A remnant also

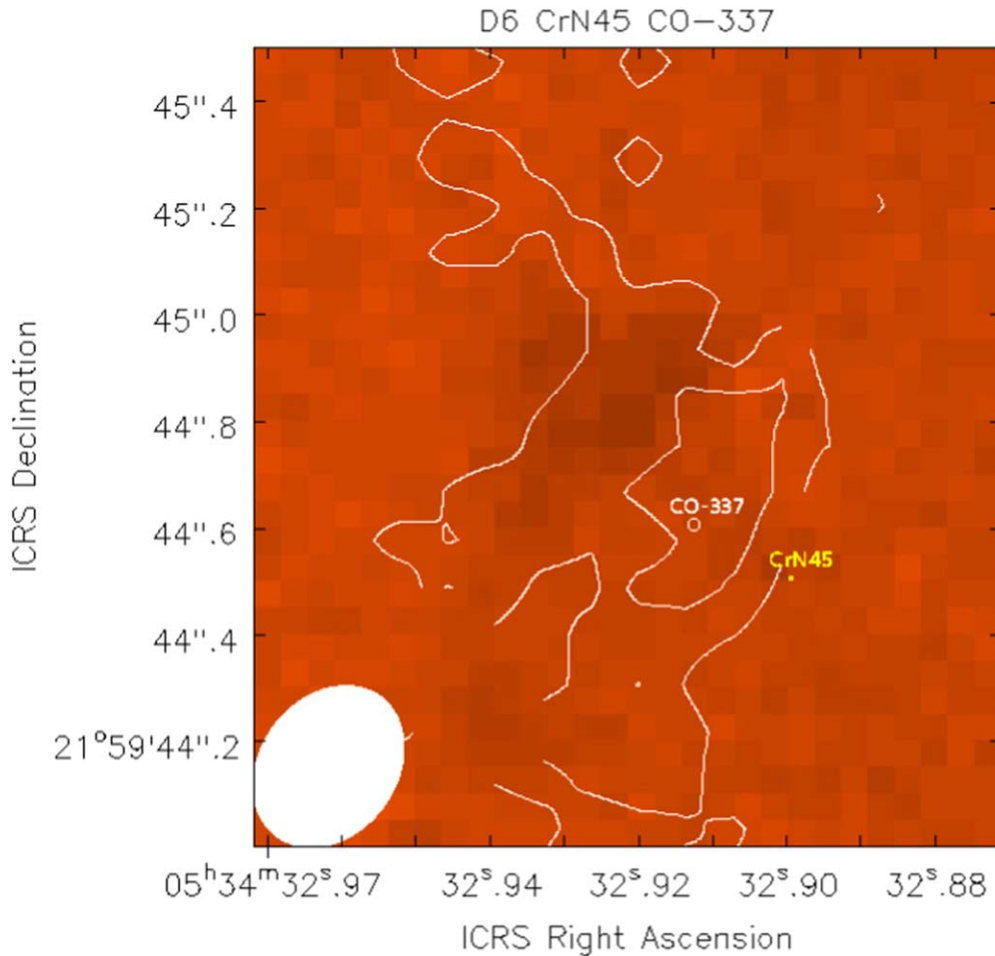


Figure 10. HST (observation GO-13510) image of the CrN45 globule near the edge of our D6 pointing field with ALMA moment 0 images of the CO velocity component at $V_{\text{LSRK}} = -337 \text{ km s}^{-1}$. Contours are as in Figure 2.

showed emission from cool CO, HCO^+ , SiO, and SO molecules, possibly from post-explosion elemental mixing.

Eight of the clouds showing CO emission, including Knot 51, were found to be associated with absorption patches identified against the nebular emission as cataloged by Grenman et al. (2017). Four CO emission regions were not identified with absorption or with H_2 emission features. Some H_2 emitting knots showed no associated CO (e.g., Knot 50) while some prominent absorption patches did not show detectable CO emission (e.g., CrN18).

For the obscuring clouds, Grenman et al. (2017) provided estimates of visual absorption, which we have used to estimate the total column of H_2 . Using assumptions for the excitation of CO, SiO, HCO^+ , and SO based on Richardson et al. (2013) models we estimated molecular column densities. The models do not predict substantial warm CO, consistent with nondetection of higher-J CO lines in the much lower resolution Barlow et al. (2013) SPIRE FTS spectra. Abundances derived from the comparison of H_2 and molecular columns suggest that these globules are chemically similar to the diffuse interstellar medium. Therefore, in the thousand years since the supernova which produced the Crab Nebula, chemical processes have produced a molecular retinue similar to those seen in regions of presumably far more advanced age. For the few younger remnants for which there is data, a similar collection of molecules have been identified (Matsuura et al. 2017).

Molecules can therefore provide good estimators of physical conditions within newly identified cool and dense clumps within the evolving remnant.

Other regions, like the helium-rich belt, have very different compositions. The Crab is probably also not chemically homogeneous in the molecular knots that are the focus of this work. Deep ALMA and JWST observations of these anomalous regions should be a high priority for future work.

The optical, IR, and now submillimeter observations suggest that the globules have a common geometry with a cool molecular core that is detected in CO, surrounded by a warmer molecular layer emitting H_2 . These are encased in an envelope of ionic emission seen in the HST images. Individual knots are a combination of these basic ingredients, with different amounts of each in different knots. This shows that a surprisingly simple basic geometry can account for what appears overly complex.

The Richardson et al. (2013) study focused on understanding the near-IR H_2 emission and was not guided by the type of submillimeter observations now possible with ALMA. Nonetheless, they postulated that globules with fully molecular cores were likely, although they would be too cool to contribute to the observed H_2 emission. The CO and other submillimeter lines we detect strongly support the existence of such a fully molecular core in some globules although it is not possible to identify the heating mechanism. The low-J CO lines are

Table 4
Observed Relative Abundances in the Crab SNR Molecular Globules

Field	Transition Line	X Column Density cm ⁻²	H ₂ Column Density cm ⁻²	Abundance Estimate n(X)/nH
Kn51/CrN12	CO 3-2	$(5.5 \pm .2) \times 10^{15}$	7.5×10^{21}	$7. \times 10^{-7}$
Kn53/CrN16	CO 3-2	$(1.7 \pm .1) \times 10^{16}$	2.7×10^{22}	$7. \times 10^{-7}$
Kn53/CrN17	CO 3-2	$(1.5 \pm .1) \times 10^{16}$	1.4×10^{21}	1.1×10^{-5}
Kn53/CrN18	CO 3-2	$(1.1 \pm .1) \times 10^{15}$	7.1×10^{21}	1.6×10^{-7}
Kn53/CrN20W	CO 3-2	$(1.6 \pm .7) \times 10^{16}$	9.4×10^{20}	3.1×10^{-5}
Kn53/CrN22	CO 3-2	$(1.3 \pm .2) \times 10^{16}$	7.1×10^{21}	1.6×10^{-7}
Kn51/CrN45	CO 3-2	$(5.5 \pm .2) \times 10^{15}$	4.1×10^{20}	1.7×10^{-5}
Kn51/CrN12	HCO ⁺ 4-3	$(5 \pm .4) \times 10^{12}$	7.5×10^{21}	7×10^{-10}
Kn53/CrN16	HCO ⁺ 4-3	$(8 \pm .4) \times 10^{12}$	1.4×10^{21}	6×10^{-9}





thermalized so mainly determine the temperature. Other diagnostics, not available to the Richardson et al. (2013) study and so not predicted by them, should reveal the energy source for the molecular cores. These should be the focus of future studies.

The geometry and spectra of Crab Nebula filaments are eerily similar to the filaments seen in cool-core clusters of galaxies (Fabian et al. 2008; Ferland et al. 2009; Fabian et al. 2011). Indeed, this was the original motivation for the Richardson et al. (2013) study, as they explain. Even the gas pressures are analogous, with $nT \sim 2 \times 10^6 \text{ cm}^{-3} \text{ K}$ for Knot 51 in the Crab and $\sim 3 \times 10^6 \text{ cm}^{-3} \text{ K}$ for well-studied regions of the Perseus cluster. Only some differences might be noted: the metallicity of the gas is higher in the Crab filaments, being expelled by the massive central star, while the cooling gas in clusters is a mixture of primordial gas and ejecta from the central galaxy. The gas metallicity in the Perseus cluster is estimated to be 0.3 solar (Sanders et al. 2004). Dust is forming in supernovae ejecta (Sarangi et al. 2018), while it has difficulty surviving the sputtering in clusters (Draine & Salpeter 1979). The similarities in the gas excitation provided the original motivation to understand the far closer Crab Nebula filaments. Ferland et al. (2009) argued that the cluster filaments are excited by energetic particles mixing with atomic and molecular gas. Our current work shows that this process accounts for the emission from cool dense regions of Crab globules as well. The bright and well spatially resolved Crab Nebula thus provides a laboratory to understand nearby analogs of the cool-core cluster environment.

The late Ed Loh played an important role in initiating this work. We thank the referee for their very helpful and detailed comments. The National Radio Astronomy Observatory is a facility of the National Science Foundation operated under cooperative agreement by Associated Universities, Inc. This paper makes use of the following ALMA data: ADS/JAO.ALMA2015.1.00188.S. ALMA is a partnership of ESO (representing its member states), NSF (USA), and NINS (Japan), together with NRC (Canada), MOST, and ASIAA (Taiwan), and KASI (Republic of Korea), in cooperation with the Republic of Chile. The Joint ALMA Observatory is operated by ESO, AUI/NRAO, and NAOJ. Rory Bentley was a summer student at the National Radio Astronomy Observatory. G.J.F. acknowledges support by NSF (1816537,

1910687), NASA (ATP 17-ATP17-0141, 19-ATP19-0188), and STScI (HST-AR- 15018 and HST-GO-16196.003-A).

ORCID iDs

Alwyn Wootten  <https://orcid.org/0000-0001-7026-6099>
A. C. Fabian  <https://orcid.org/0000-0002-9378-4072>
G. J. Ferland  <https://orcid.org/0000-0003-4503-6333>
C. N. Shingledecker  <https://orcid.org/0000-0002-5171-7568>

References

- Barlow, M. J., Krause, O., Swinyard, B. M., et al. 2010, *A&A*, 518, L138
Barlow, M. J., Swinyard, B. M., Owen, P. J., et al. 2013, *Sci*, 342, 1343
De Looze, I., Barlow, M. J., Bandiera, R., et al. 2019, *MNRAS*, 488, 164
De Looze, I., Barlow, M. J., Swinyard, B. M., et al. 2017, *MNRAS*, 465, 3309
Draine, B. T., & Salpeter, E. E. 1979, *ApJ*, 231, 77
Dubner, G., Castelletti, G., Kargaltsev, O., et al. 2017, *ApJ*, 840, 82
Fabian, A. C., Johnstone, R. M., Sanders, J. S., et al. 2008, *Natur*, 454, 968
Fabian, A. C., Sanders, J. S., Williams, R. J. R., et al. 2011, *MNRAS*, 417, 172
Ferland, G. J., Fabian, A. C., Hatch, N. A., et al. 2008, *MNRAS*, 386, L72
Ferland, G. J., Fabian, A. C., Hatch, N. A., et al. 2009, *MNRAS*, 392, 1475
Gomez, H. L., Krause, O., Barlow, M. J., et al. 2012, *ApJ*, 760, 96
Graham, J. R., Wright, G. S., & Longmore, A. J. 1990, *ApJ*, 352, 172
Grennan, T., Gahm, G. F., & Elfgren, E. 2017, *A&A*, 599, A110
Hester, J. J., Graham, J. R., Beichman, C. A., & Gautier, T. N., III 1990, *ApJ*, 357, 539
Ivlev, A. V., Dogiel, V. A., Chernyshov, D. O., et al. 2018, *ApJ*, 855, 23
Kamenetzky, J., McCray, R., Indebetouw, R., et al. 2013, *ApJL*, 773, L34
Liszt, H. S. 2007, *A&A*, 461, 205
Loh, E. D., Baldwin, J. A., Curtis, Z. K., et al. 2011, *ApJS*, 194, 30
Loh, E. D., Baldwin, J. A., & Ferland, G. J. 2010, *ApJL*, 716, L9
Loh, E. D., Baldwin, J. A., Ferland, G. J., et al. 2012, *MNRAS*, 421, 789
Matsuura, M., Indebetouw, R., Woosley, S., et al. 2017, *MNRAS*, 469, 3347
Owen, P. J., & Barlow, M. J. 2015, *ApJ*, 801, 141
Padovani, M., Galli, D., Ivlev, A. V., Caselli, P., & Ferrara, A. 2018, *A&A*, 619, A144
Priestley, F. D., Barlow, M. J., & Viti, S. 2017, *MNRAS*, 472, 4444
Rho, J., Gomez, H. L., Boogert, A., et al. 2018, *MNRAS*, 479, 5101
Richardson, C. T., Baldwin, J. A., Ferland, G. J., et al. 2013, *MNRAS*, 430, 1257
Sanders, J. S., Fabian, A. C., Allen, S. W., & Schmidt, R. W. 2004, *MNRAS*, 349, 952
Sarangi, A., Matsuura, M., & Micelotta, E. R. 2018, *SSRv*, 214, 63
Shaw, G., & Ferland, G. J. 2021, *ApJ*, 908, 138
Shaw, G., Ferland, G. J., & Ploeckinger, S. 2020, *RNAAS*, 4, 78
Temim, T., Dwek, E., Arendt, R. G., et al. 2017, *ApJ*, 836, 129
van der Tak, F. F. S., Black, J. H., Schöier, F. L., Jansen, D. J., & van Dishoeck, E. F. 2007, *A&A*, 468, 627
Wallström, S. H. J., Biscaro, C., Salgado, F., et al. 2013, *A&A*, 558, L2